Article

The Design of Cone and Pendulum Scanning Mode Using Dual-Camera with Multi-Dimensional Motion Imaging Micro-Nanosatellite

Zheng Zhi [1,2,3], Hongsong Qu [4,*], Shuping Tao [1,3], Liangliang Zheng [1,3], Shipeng Ying [1,2,3] and Heqian Zhu [1,2,3]

[1] Changchun Institute of Optics, Fine Mechanics and Physics (CIOMP), Chinese Academy of Sciences, Changchun 130033, China
[2] University of Chinese Academy of Sciences, Beijing 100049, China
[3] Key Laboratory of Space-Based Dynamic Rapid Optical Imaging Technology, Chinese Academy of Sciences, Changchun 130033, China
[4] Research Center for Intelligent Sensing Systems, Zhejiang Laboratory, Hangzhou 311100, China
[*] Correspondence: quhongsong@zhejianglab.com

Abstract: This paper focuses on the design of a new optical cone and pendulum scanning imaging mode for micro-nanosatellites. This kind of satellite uses a high-resolution camera with a small imaging plane to achieve high-resolution and ultra-wide coverage imaging through the three-dimensional motion of the camera's wobble, satellite spin, and satellite orbital motion. First, this paper designs a single-camera constant speed OCPSI (optical cone and pendulum scanning imaging) mode. On the premise of ensuring coverage, the motion parameters and imaging parameters are derived. Then, in order to improve the performance and imaging quality of the system, a dual-camera variable speed OCPSI mode is designed. In this method, in order to reduce the overlap ratio, the camera is oscillated at a variable speed. Turn on the cameras in turn at the same time to minimize the overlap. This paper details these working modes. The simulation experiment is carried out using the satellite orbit of 500 km, the focal length of 360 mm, the pixel size of 2.5 μm, the resolution of [5120 × 5120], the number of imaging frames in the pendulum scanning hoop of 10, and the initial camera inclination angle of 30°. The single-camera constant speed OCPSI mode has an effective swath of 1060 km at a ground sampling distance of 5.3 m. The dual-camera variable speed OCPSI mode has an effective width of 966 km under the same conditions. Finally, the ground experiment prototype of OCPSI imaging theory is designed. We choose a camera with a pixel size of 3.45 μm, a resolution of [1440 × 1080], and a focal length of 25 mm. The ground experiment was carried out at the initial camera inclination angle of 10°, the number of imaging frames in the pendulum scanning hoop of 3, and the orbit height of 11 m. The experimental result is that the effective width of OCPSI imaging mode reaches 10.8 m. Compared with the traditional push-broom mode using the same camera, the effective width of 1.64 m is increased by seven times, and the effective width of 3.83 m is increased by three times compared to the traditional whisk-broom imaging mode. This study innovatively integrates three-dimensional motion imaging into aerospace remote sensing and provides a reference for the research on the realization of high-resolution and ultra-wide coverage of micro-nano remote sensing satellites.

Keywords: remote sensing; high resolution; wide-swath imaging; optical imaging; cone and pendulum scanning; micro-nanosatellite

1. Introduction

Ground resolution, ground coverage width, and payload weight are three key indicators of spaceborne remote sensing. Ground resolution is the sharpness of the image, which determines the spatial resolution of remote sensing satellites. The ground coverage width is the vertical orbit coverage width under the condition of single orbit, which determines the

time resolution of remote sensing satellites. The payload weight determines the capability of the satellite platform. These three indicators are actually mutually restrictive, and to guarantee two indicators, the other must be sacrificed [1].

From the perspective of spaceborne remote sensing, improving the cost-effectiveness of Earth observation missions on the basis of satisfying information needs is the development goal of space remote sensing. The improvement of various indicators of small satellites makes small satellites gradually replace the status of large satellites in some missions. According to the simplified definition proposed by The International Academy of Astronautics (IAA) more than 30 years ago, a satellite weighing less than 1000 kg is a small satellite, as shown in Figure 1 [2]. Small satellite missions are primarily accomplished in two ways. One approach is to focus on a single mission, using multiple small satellites for constellation networking. Another method is to make full use of the developing technology to design new payloads with outstanding characteristics to complete high-performance Earth observation missions.
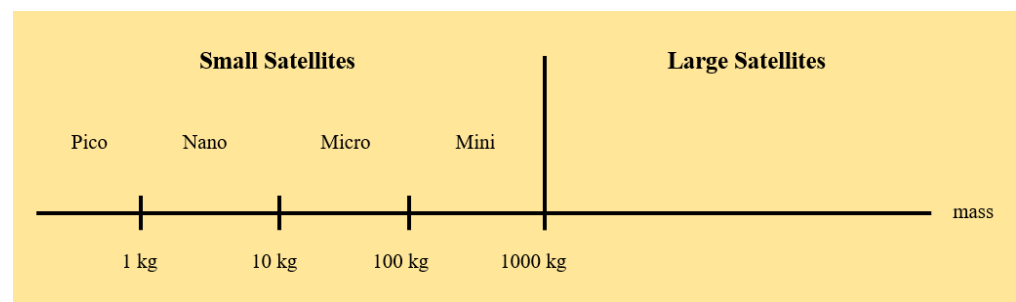
Figure 1. The satellite differentiation standard based on mass.

However, in some Earth observation missions, a certain amount of ground resolution is selectively sacrificed in order to ensure the coverage width. Some common Earth observation missions and resolutions in practical missions are shown in Figure 2 [3]. Therefore, in order to be competent for more tasks, how to greatly increase the ground coverage width under the premise of ensuring high resolution is a particularly important issue. There are currently three mainstream wide-swath imaging methods: multi-sensor inner field of view (FOV) stitching, multi-camera outer FOV stitching, and agile imaging based on satellite maneuverability.
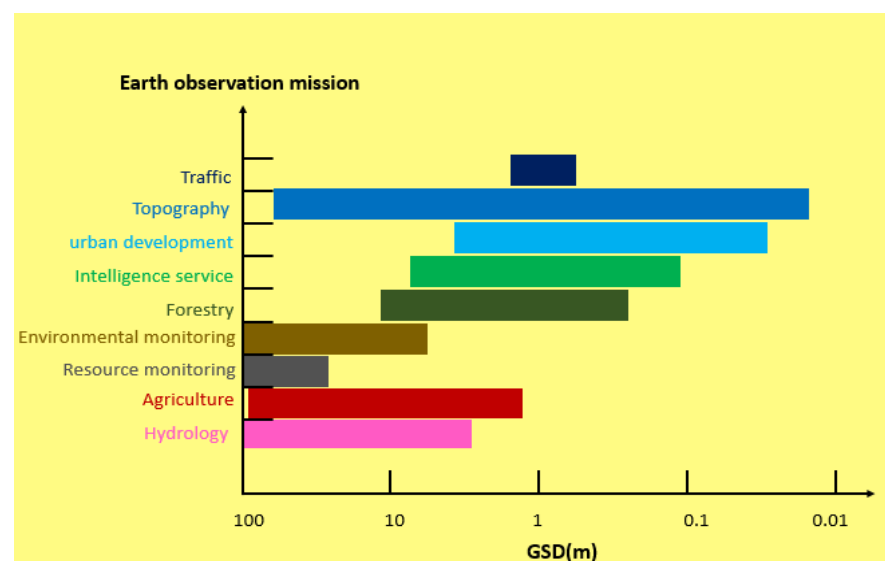
Figure 2. Common Earth observation missions and their resolution in practical missions.

Multi-sensor inner FOV stitching is the most widely used imaging method, especially in push-broom imaging modes using linear CCDs. In order to enlarge the swath width, splicing of CCDs is usually required. The traditional method of multi-sensor inner FOV stitching is direct stitching, and the detector is used for FOV stitching. Due to the limitation of physical factors such as the structure of the detector and the outer packaging of the device, it is difficult to arrange the CCDs directly in a line, so the multi-sensor inner FOV stitching requires a stitching algorithm to obtain continuous and seamless remote sensing images [4,5]. For example, the QuickBird satellite launched by the United States in 2001 was the first commercial satellite in the world to offer sub-meter resolution products. The camera is composed of 6 CCDs staggered and stitched, and can obtain images with a resolution of 0.61 m and a wide swath of 16.5 km [6]. The Wide Field of View Camera (WFV) carried by the Gaofen-6 (GF-6) satellite launched by China in 2018 can cover 800 km on a single track and has a resolution of 16 m, which is the highest level of observation width among similar satellites in the world. WFV is stitched by eight pieces of complementary metal oxide semiconductors (CMOSs) and uses an off-axis four-mirror optical system to obtain a large FOV of 65.64° [7]. The new method of multi-sensor inner FOV stitching is indirect stitching, which uses reflection and transmission to split the FOV into multiple CCDs. For example, the ZY-3 satellite uses a half-mirror to stitch three CCDs together, and a product with a resolution of 2–5 m and a width of 50 km can be obtained [8]. Multi-sensor inner FOV stitching has the advantages of expanding the FOV and increasing the coverage width while ensuring high resolution, but it is easily affected by factors such as focal plane stitching errors, camera optical system distortion, and satellite attitude changes.

In order to increase the ground coverage width to a greater extent, the remote sensing satellite adopts the multi-camera outer FOV stitching method. The traditional multi-camera outer FOV stitching method is to install multiple cameras on the same satellite platform with overlapping FOV. For example, the Gaofen-1 (GF-1) satellite launched in 2013, as the first satellite of China's high-resolution Earth observation system, is equipped with two cameras with a resolution of 2 m (panchromatic)/8 m (multispectral). Images with the ground coverage width of 60 km can be obtained by outer FOV stitching. In addition, the satellite is also equipped with four wide FOV cameras (WFV) with a resolution of 16 m installed in vertical orbits, which can obtain an image with a width of 800 km after the outer FOV is stitched [9–11]. The main disadvantages of the multi-camera outer FOV stitching method are the requirements on satellite platform performance, payload weight, and cost. These problems make the method unsuitable for small satellites. With the improvement of the performance of micro-nanosatellites, it is proposed to use the images obtained by multiple satellites of the constellation to stitch together to increase the ground coverage width. For example, Planet Labs launched a large constellation of 3U cubesats, also known as pigeons, with more than 150 currently in orbit. The Flock satellite constellation utilizes differential drag control to complete coverage imaging of the Earth every day with a resolution of 3.7 m [12,13]. However, this approach requires complex satellite deployment and mission mobilization to reduce overlap [14,15].

Using satellite agile maneuverability to perform planned multi-strip stitching imaging is a new wide-swath imaging method brought by the development of agile satellites. The high-resolution optical remote sensing satellites in the United States are basically agile satellites, which use high maneuverability to increase the single-track wide swath of high-resolution satellites. For example: GeoEye satellites and WorldView satellites [16]. In addition, France's Pleiades satellite [17] and China's SuperView-1 satellite [18] are also agile satellites with high maneuverability. Take the SuperView-1 satellite as an example. The high-resolution camera (panchromatic 0.5 m/multispectral 2 m) carried on the SuperView-1 satellite has a width of only 12 km, but it can achieve stitching imaging of up to 5 strips, covering an area of 60 km × 70 km. This method places high demands on the maneuverability of the satellites and requires a lot of mission planning and scheduling.

In summary, multi-sensor inner field of view stitching, multi-phase outer field of view stitching and agile imaging based on satellite maneuverability all have their own

advantages, but they all fail to solve the mutual constraints of ground resolution, ground coverage width, and load weight. Under the premise of ensuring high resolution and ultra-large width, there is an urgent need for a new imaging mode that reduces costs. Referring to the foreign microwave cone scanning imager [19–24], we propose a novel optical cone and pendulum scanning imaging mode. The method uses a single-detector optical area array camera to perform frame stitching imaging by using camera swing and satellite spin motion. There are also more precise control methods to support the satellite spin motion [25]. In this paper, firstly, a single-camera constant speed optical cone and pendulum scanning imaging mode is designed. Under the condition of ensuring ground coverage, the satellite's uniform spinning motion and the camera's uniform oscillating motion are used to derive the angular velocity of the satellite cone scanning and the angular velocity of the camera pendulum scanning. In order to improve the system performance, a dual-camera variable speed optical cone and pendulum scanning imaging mode is proposed. This method can more reasonably plan the coverage of each frame of images by adjusting the angular velocity of the camera pendulum scanning in real time, reduce the amount of data, lower the requirements for the attitude control capability of the satellite platform, and obtain higher-quality original images. These two novel operating modes are described in detail in this paper and simulated. Finally, the ground principle prototype is designed and ground verification experiments are carried out.

The remaining of this paper is organized as the following: Section 2 proposes the optical cone and pendulum scanning imaging method and introduces the process of parameter design. Section 3 introduces the design methods of the two imaging modes according to the flowchart and deduces the relevant formulas in detail. Section 4 simulates and verifies two imaging modes and completes the ground verification experiments. Section 5 concludes this paper and proposes possible future research directions.

2. Optical Cone and Pendulum Scanning Imaging Method

The principle of OCPSI (optical cone and pendulum scanning imaging) is illustrated in Figure 3, taking a single camera as an example. The OCPSI satellite operates on a circular low orbit, with V_s. being the velocity of the satellite. The optical camera composed of single CMOS has an initial inclination angle before booting, and the optical axis and the nadir axis form an inclination angle α. During the imaging of the camera, the satellite rotates continuously around the nadir axis with an angular velocity ω_s. As shown in Figure 3, multiple frames of images are formed into a coverage area within the T_1 time interval. The camera rotates continuously around the main point of the camera with an angular velocity ω_c to form a coverage area. The imaging sequence of a coverage area is shown in Figure 4. The time interval T during which the satellite rotates once is the cone scanning period. The time interval T_{out} during which the camera oscillates once is the pendulum scanning period. Under the coupled motion condition of satellite rotation and camera pendulum, the camera ground trajectory of the OCPSI remote sensing satellite can completely cover the ground. There are many control strategies, which prove the possibility of attitude control of OCPSI satellites. For example, the quaternion-based feedback control law proposed by Wu et al. and two reaction wheels mounted in a V shape proposed by Ousaloo can be used for attitude control of a satellite rotation [26,27].

From the camera image plane to the ground target, it needs to go through four coordinate frame for mapping.

In Figure 4, the image plane coordinate frame $o_p x_p y_p z_p$ is defined as follows:

1. The origin o_p is the center of the camera image plane;
2. The z_p axis coincides with the optical axis of the camera and points to the ground;
3. The y_p axis is perpendicular to the z_p axis in the camera image plane, pointing to the opposite of the satellite movement direction;
4. The x_p axis is perpendicular to the plane formed by the camera optical axis and the y_p axis and forms a right-handed coordinate frame with the y_p axis and the z_p axis.
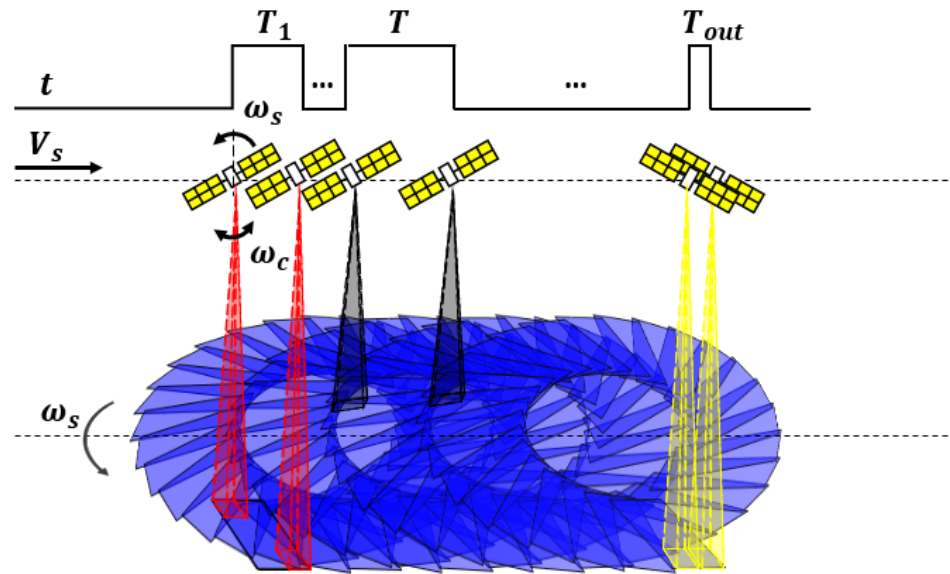
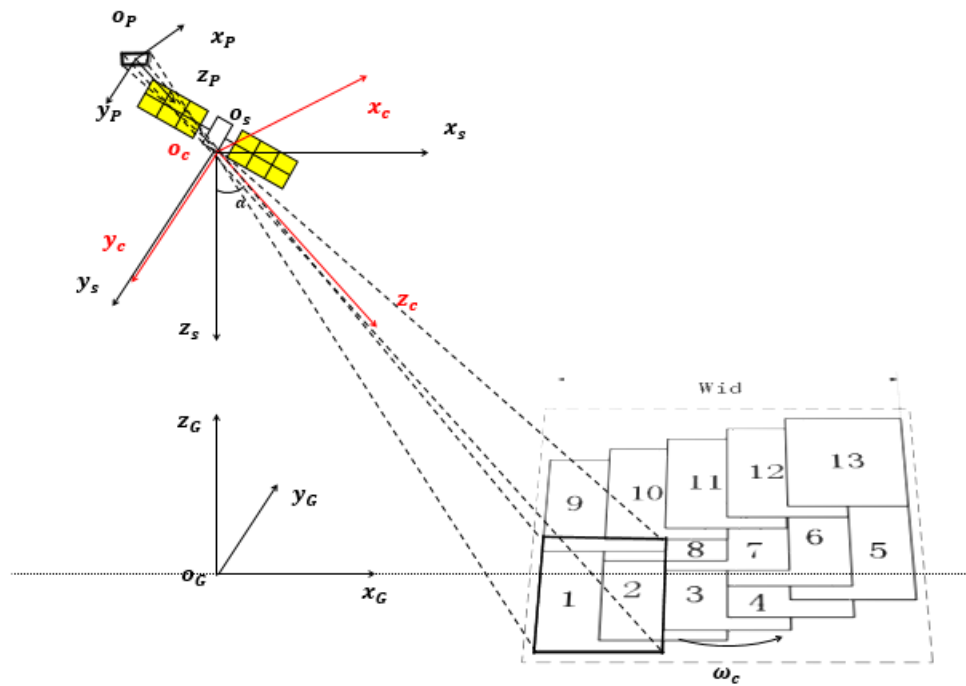**Figure 3.** Illustration of an OCPSI satellite.

Figure 4. OCPSI axis mapping.

The camera coordinate frame $o_c x_c y_c z_c$ is defined as:

1. The origin o_c is the intersection of the camera optical axis and the nadir axis;
2. The z_c axis coincides with the camera optical axis and points to the ground;
3. The y_c axis is perpendicular to the z_c axis and points to the opposite direction of the satellite movement direction;
4. The x_c axis is perpendicular to the plane composed of the camera optical axis and the y_c axis, forming a right-hand coordinate frame with the y_c axis and the z_c axis.

The satellite coordinate frame $o_s x_s y_s z_s$ is defined as:

1. The origin o_s is the intersection point of the camera optical axis and the nadir axis;
2. The z_s axis coincides with the nadir axis and points to the ground;

3. The y_s axis is perpendicular to the z_s axis and points to the opposite direction of the satellite movement direction;

4. The x_s axis is perpendicular to the plane formed by the camera optical axis and the y_s axis, forming a right-handed coordinate frame with the y_s axis and the z_s axis.

The geographic coordinate frame $o_G x_G y_G z_G$ is defined as:

1. The origin o_G is the intersection of the nadir axis and the ground;

2. The z_G axis coincides with the zenith axis and points to the zenith;

3. The y_G axis is perpendicular to the z_G axis and points to the direction of satellite motion;

4. The x_G axis is perpendicular to the plane formed by the optical axis of the camera and the y_G axis and forms a right-hand coordinate frame with the y_G axis and the z_G axis.

Then, from the pixel on the image plane coordinate frame to the target point in the geographic coordinate frame can be represented by:

$$
\begin{bmatrix} X_G \\ Y_G \\ Z_G \\ 1 \end{bmatrix} = C_s^G \begin{bmatrix} X_s \\ Y_s \\ Z_s \\ 1 \end{bmatrix} = C_s^G C_c^s \begin{bmatrix} X_c \\ Y_c \\ Z_c \\ 1 \end{bmatrix} = C_s^G C_c^s C_p^c \begin{bmatrix} X_p \\ Y_p \\ Z_p \\ 1 \end{bmatrix} \tag{1}
$$

where the image plane coordinate frame needs to translate f along the positive direction of the z_p axis to the camera coordinate frame, and the transformation matrix is C_p^c. From the camera coordinate frame to the satellite coordinate frame, it needs to rotate the angle γ around the y_c axis and enlarges it by $\frac{H}{f}$ times, and its transformation matrix is C_c^s. From the satellite coordinate frame to the geographic coordinate frame, it needs to translate H along the negative direction of the z_s axis and rotate $180°$ around the x_s axis, and the change matrix is C_s^G. The three transformation matrices satisfy

$$
C_p^c = \begin{bmatrix} 1 & 0 & 0 & 0 \\ 0 & 1 & 0 & 0 \\ 0 & 0 & 1 & f \\ 0 & 0 & 0 & 1 \end{bmatrix}
$$

$$
C_c^s = \begin{bmatrix} \frac{H}{f} & 0 & 0 & 0 \\ 0 & \frac{H}{f} & 0 & 0 \\ 0 & 0 & \frac{H}{f} & 0 \\ 0 & 0 & 0 & 1 \end{bmatrix} \begin{bmatrix} cos\gamma & 0 & -sin\gamma & 0 \\ 0 & 1 & 0 & 0 \\ sin\gamma & 0 & cos\gamma & 0 \\ 0 & 0 & 0 & 1 \end{bmatrix}
$$

$$
C_s^G = \begin{bmatrix} 1 & 0 & 0 & 0 \\ 0 & 1 & 0 & 0 \\ 0 & 0 & 1 & -H \\ 0 & 0 & 0 & 1 \end{bmatrix} \begin{bmatrix} 1 & 0 & 0 & 0 \\ 0 & cos\pi & sin\pi & 0 \\ 0 & -sin\pi & cos\pi & 0 \\ 0 & 0 & 0 & 1 \end{bmatrix}
$$

where f is the camera focal length. H is the satellite orbital altitude. γ is the angle between the camera optical axis and the nadir axis, including the initial tilt angle α and the camera swing angle β. Then, the projection of the image plane on the Earth can be calculated recursively according to $[X_G, Y_G, Z_G]^T$, and the position of the satellite on the Earth-centered Earth-fixed (ECEF) coordinate system. Equation (1) will be used in subsequent simulations.

Next, we design the basic parameters through geometric analysis, as shown in Figures 5 and 6. First, FOV is the field of view of the camera, which is determined by the detector surface size L and the focal length f of the camera. The detector area size is determined by the pixel size a and the number of pixels $n_1 \times n_2$. Then, FOV can be expressed as

$$
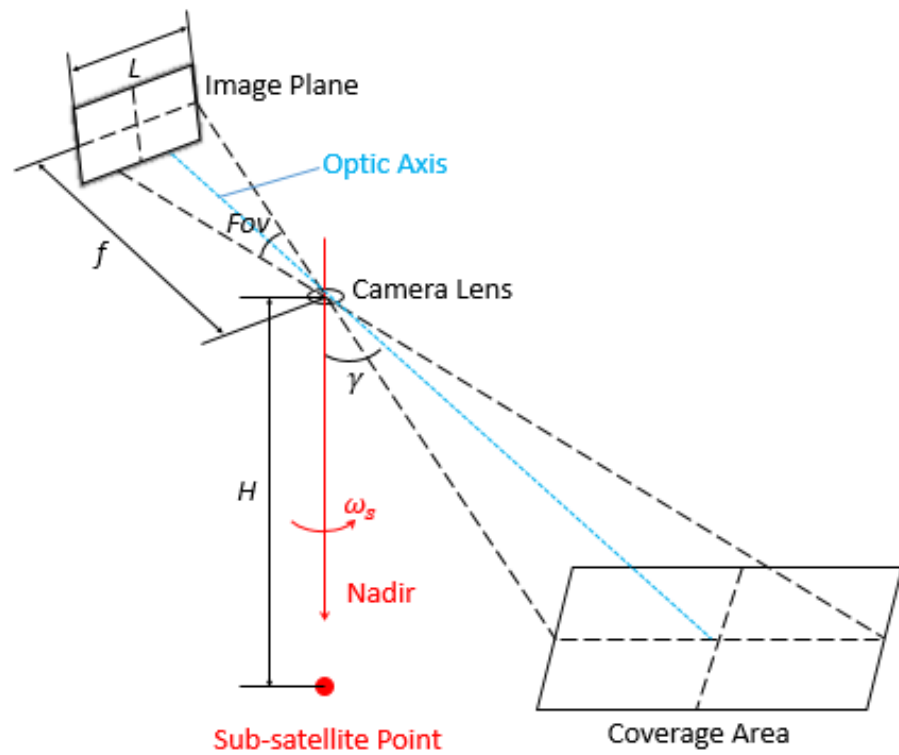FOV = 2arctan\left(\frac{L}{2f}\right) = 2\arctan\left(\frac{a \times n_1}{2f}\right) \tag{2}
$$

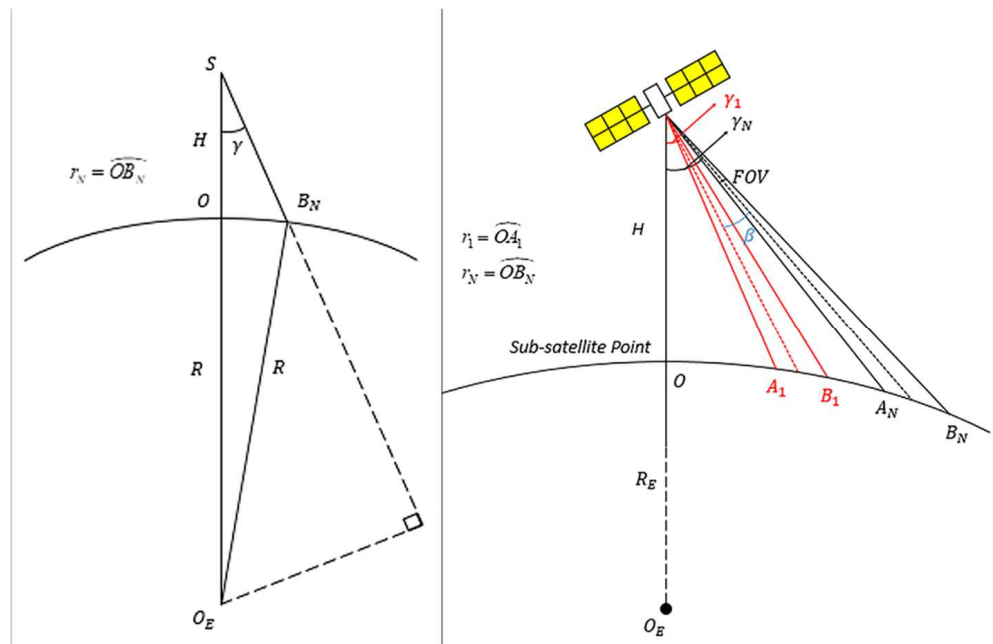**Figure 5.** Mapping of the image plane to the Earth.

Figure 6. The actual mapping at a large width.

As shown in Figure 6, according to the user's requirements for ground coverage width and ground resolution, the camera parameters such as the image plane size *L*, field of view angle *FOV*, focal length *f*, and satellite parameters such as satellite height *H* and camera tilt angle γ are determined. Different from traditional imaging with a small field of view, under the condition of ultra-large width of thousand kilometers, the ground needs to be

regarded as a sphere. Then design the ground cover width $2r_N$ according to the triangular relationship as

$$\frac{\sin\left(\frac{r_N}{R}\right)}{SB_N} = \frac{\sin\left(\gamma_N + \frac{FOV}{2}\right)}{R} \tag{3}$$

where the angle between the optical axis of the camera and the nadir axis is $\gamma_N = \alpha + \beta_{max}$, R is the radius of the Earth, and SB_N is expressed by

$$SB_N = (R + H)\cos(\gamma) - \sqrt{R^2 - [(R+H)\sin(\gamma)]^2} \tag{4}$$

At the same time, r_1 can also be calculated by the law of sine as

$$\frac{\sin\left(\frac{r_1}{R}\right)}{SA_1} = \frac{\sin(\gamma_1)}{R} \tag{5}$$

It can be further rewritten by substituting Equation (4) into Equation (3) as

$$r_N = R\arcsin\left(\frac{\left\{(R+H)\cos\left(\gamma_N + \frac{FOV}{2}\right) - \sqrt{R^2 - \left[(R+H)\sin\left(\gamma_N + \frac{FOV}{2}\right)\right]^2}\right\} * \sin\left(\gamma_N + \frac{FOV}{2}\right)}{R}\right) \tag{6}$$

Similarly, Equation (5) can also be rewritten as

$$r_1 = R\arcsin\left(\frac{\left\{(R+H)\cos\left(\gamma_1 - \frac{FOV}{2}\right) - \sqrt{R^2 - \left[(R+H)\sin\left(\gamma_1 - \frac{FOV}{2}\right)\right]^2}\right\} * \sin\left(\gamma_1 - \frac{FOV}{2}\right)}{R}\right) \tag{7}$$

Geometrically, r_N is the radius from the satellite sub-satellite point to the outer boundary of the image, r_1 is the radius from the satellite sub-satellite point to the inner boundary of the image, and the ring formed by the image is filled by the single-camera swing imaging.

In order to make the ground coverage complete and leak-free in the OCPSI mode, it is necessary to ensure that the three parts overlap each other. The three parts are the overlap between two frames, the overlap between two pendulum scanning cycles, and the overlap between two cone scanning cycles. The three parameters are related to each other with the sub-satellite velocity (V_s), the satellite cone scanning velocity (ω_s) and the camera pendulum scanning velocity (ω_c), as shown in Figure 7. The satellite sub-satellite velocity (V_s) can be determined from the orbital altitude. The satellite sub-satellite velocity (V_s) can be combined with the overlap between the two cone sweep periods to obtain the satellite cone scanning velocity (ω_s). Then, according to the overlap between the two pendulum scanning periods, the sub-satellite speed (V_s) and the satellite cone scanning velocity (ω_s), the camera scanning velocity (ω_c) can be calculated. The corresponding flow chart is shown in Figure 8. In the next section, we will design reasonable parameters for the OCPSI mode according to this process.
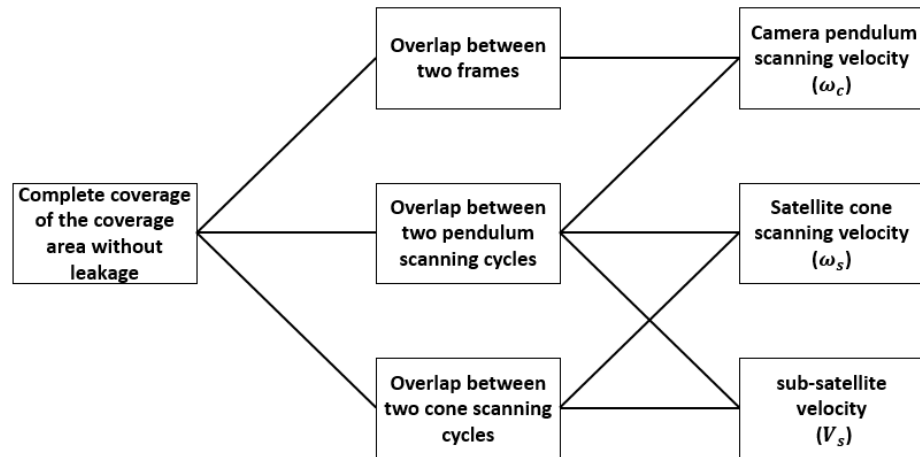
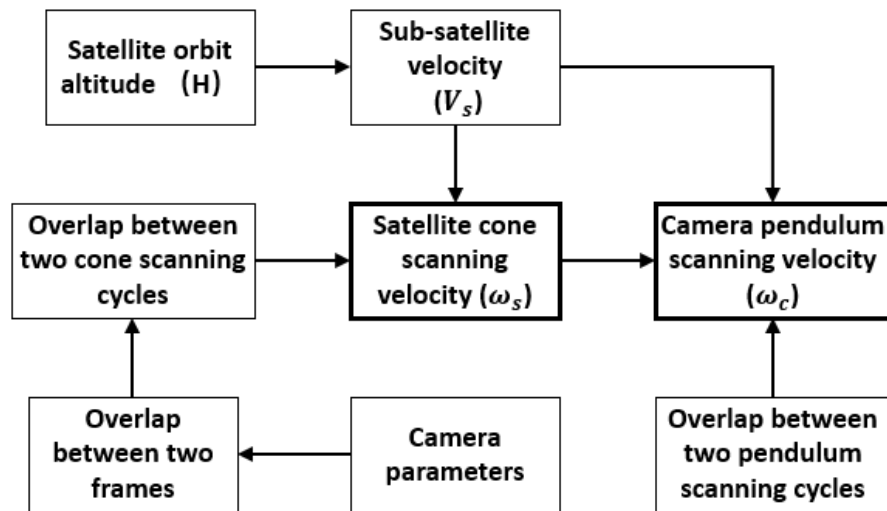**Figure 7.** Key parameter relationship diagram.

Figure 8. The design flow chart of these three motion parameters.

3. The Design of OCPSI Mode

In this section, we design the single-camera constant speed OCPSI mode and the dual-camera variable speed OCPSI mode. We focus on how to rationally design pattern parameters and the advantages of patterns while ensuring complete coverage and analyze and optimize them. We first divide the cone-scanning hoop into two parts, as shown in Figure 9. The half-ring in the direction of satellite motion is Semi-ring I, and the other half ring in the opposite direction of satellite motion is Semi-ring II.

Only the cone scanning motion is considered, and the image coverage area formed by one pendulum scanning cycle imaging is a square in Figure 9. In the figure, the hoop width is

$$d_{hoop} = r_N - r_1 \tag{8}$$

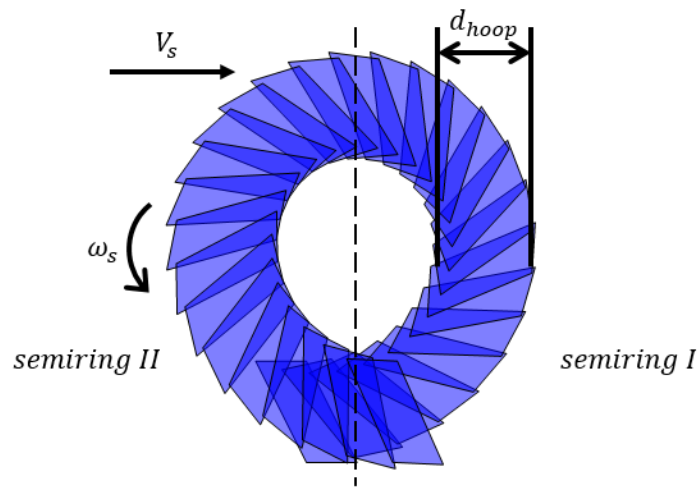where r_N and r_1 are given by Equations (6) and (7).

Figure 9. Region division of a ring.

3.1. Single-Camera Constant Speed OCPSI Mode

In the single-camera cone-scanning imaging mode, the blank part of the Semiring I formed by the current cone scan can be covered by the Semiring I of the next ring. As shown in Figure 10, after a reasonable selection of the satellite's cone scanning speed ω_s, the second ring can completely cover the blank area of the first ring.
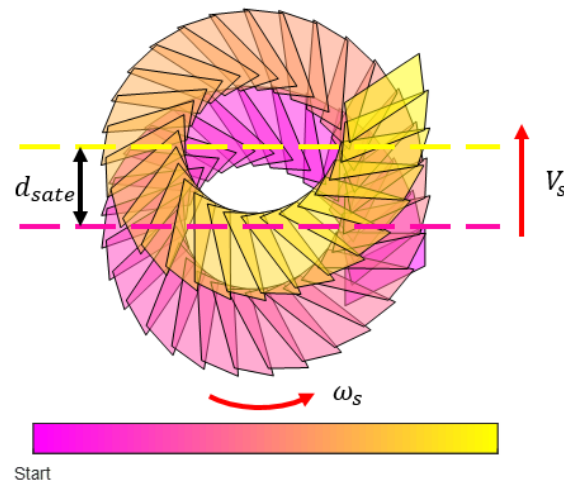

Figure 10. Blank part filling diagram.

First, we calculate the sub-satellite velocity of the satellite. In Figure 10, V_s is the relative instantaneous velocity of the satellite sub-satellite point with respect to the ground and is calculated from the orbital height H as

$$V_s = \sqrt{\frac{GM}{(R+H)}} \times \frac{R}{R+H} \qquad (9)$$

where GM is the gravitational constant.

Second, we derive the satellite cone scanning velocity from the overlap between two cone scanning cycles and the satellite sub-satellite velocity. It can be seen from Figure 10 that when the satellite cone scanning moves once, the distance traveled by the satellite sub-satellite point is d_{sate}. When the distance traveled by the sub-satellite point is equal to the width of the hoop—that is, $d_{sate} = d_{hoop}$, the image can cover the ground target perfectly. Since the hoop belt is composed of image blocks and there are jagged protrusions

on the edge of the hoop belt, the distance traveled by the satellite sub-satellite point is slightly less than the width of the hoop belt, that is

$$d_{sate} = (1 - \eta_s) \times d_{hoop} \tag{10}$$

where η_s is the overlap ratio of the width of the cone-scanning hoops. The distance d_{sate} traveled by the sub-satellite point that the satellite cone scanning has moved once is

$$d_{sate} = V_s \times T_s \tag{11}$$

where T_s is the period of the satellite cone scanning.

By Equations (8)–(11), the coverage problem of the satellite cone scanning is formulated as

$$V_s \times T_s = (1 - \eta) \times (r_N - r_1) \tag{12}$$

Therefore, the period of the satellite cone scanning and the angular velocity of the satellite cone scanning can be designed by solving the Equation (12) of the satellite cone scanning coverage problem.

$$T_s = (1 - \eta) \times \frac{(r_N - r_1)}{V_s} \tag{13}$$

$$\omega_s = \frac{2\pi}{T_s} = \frac{2\pi V_s}{(1 - \eta) \times (r_N - r_1)} \tag{14}$$

Third, we deduce the camera pendulum scanning velocity according to the satellite sub-satellite velocity, the satellite cone scanning velocity, and the overlap between two pendulum scanning cycles. We first consider pendulum motion imaging separately. In Figure 10, the image coverage area formed by imaging in one pendulum scanning period is a square, as shown in detail in Figure 11.
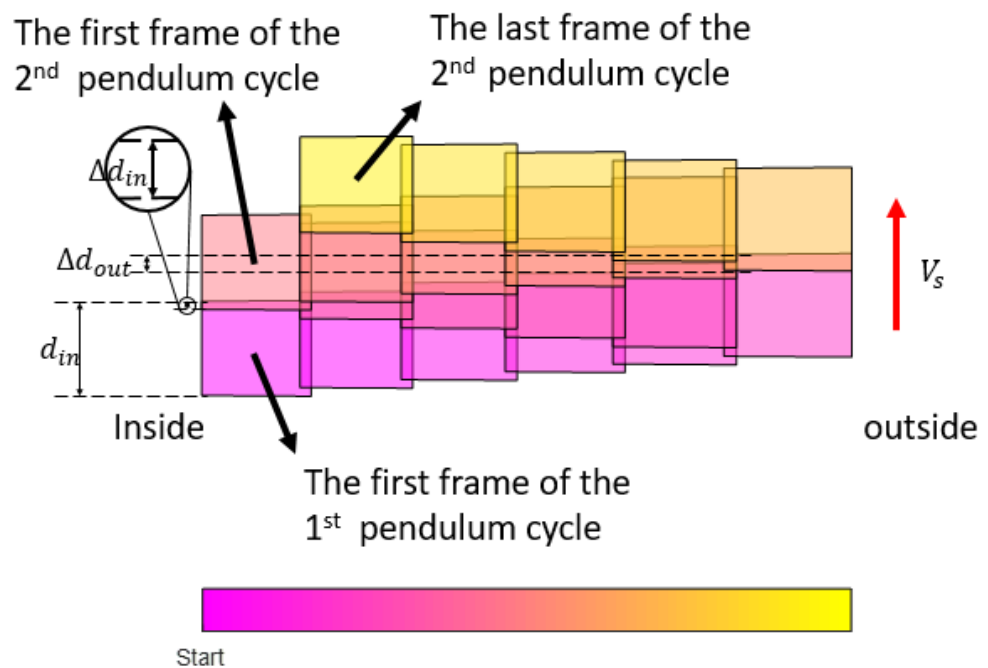

Figure 11. Image coverage in 2 pendulum cycles.

The number of image frames in a pendulum motion period is

$$f_{pend} = 2 \times (N - 1) \tag{15}$$

where N is the frame number of the hoop belt.

Since different pendulum scanning angles are generated during scanning, the ground coverage in the vertical orbit direction of each frame of image is different, so we use angle overlap to plan ground coverage. Since the pendulum scanning direction is vertical to the circumference and the direction is always changing, when the pendulum scanning speed is in the positive and negative directions along the orbit, the image movement speed is at the maximum and minimum. We perform the analysis in the vertical orbit direction. In order to ensure complete coverage and sufficient overlap of the image, we define the pendulum scanning angle overlap ratio η_{frame}:

$$\eta_{frame} = \frac{\theta_{overlap}}{FOV} \tag{16}$$

where $\theta_{overlap}$ is the overlap angle of two adjacent frames. From this, we can get the angle change of every two frames of images:

$$\Delta\theta_{frame} = \left(1 - \eta_{frame}\right) \times FOV \tag{17}$$

Then, the pendulum scanning angle of the nth frame image is expressed as

$$\beta = \begin{cases} \Delta\theta_{frame} \times rem\left(\frac{n-1}{2(N-1)}\right), & rem\left(\frac{n}{2(N-1)}\right) \leq N \\ \Delta\theta_{frame} \times \left[2(N-1) - rem\left(\frac{n-1}{2(N-1)}\right)\right], & rem\left(\frac{n}{2(N-1)}\right) > N \end{cases} \tag{18}$$

where $rem(\ )$ is the remainder.

We guarantee the coverage in the vertical orbit direction, and then, we analyze the coverage along the orbit direction. The overlap between the inside and outside of the pendulum motion imaging ensures complete ground coverage. Since there is no inclination in the orbit direction, the magnification is the same in the orbit direction. In Figure 11, the overlapping portion of the inner image Δd_{in} is significantly smaller than the overlapping portion of the outer image Δd_{out}, so we design based on the overlapping of the inner image. We define the pendulum period scanning overlap as

$$\beta\eta_{p-cycle} = \frac{\Delta d_{in}}{d_{in}} \tag{19}$$

where d_{in} is the axial width of the inner image. Therefore, the pendulum scanning period is

$$T_{pend} = \frac{(1 - \eta_{p-cycle})d_{in}}{V_s} \tag{20}$$

From this, the angular velocity of the pendulum scanning can be obtained as

$$\omega_c = \frac{2(N-1) \times \Delta\theta_{frame}}{T_{pend}} = \frac{2(N-1) \times \Delta\theta_{frame}V_s}{\left(1 - \eta_{p-cycle}\right)d_{in}} \tag{21}$$

Then, according to the above-mentioned cone scanning and pendulum scanning imaging, the OCPSI mode is a coupling of the two. The schematic diagram of the OCPSI ground coverage is shown in Figure 12. In order to simplify the derivation of the cone and pendulum scanning image, we use a set of spiral equations to describe the trajectory of the optical axis of the camera, the origin is the position of the sub-satellite point at the start time.

$$\begin{cases} x = r_i \times \cos(\theta_i), \\ y = r_i \times \sin(\theta_i) + V_s t, \end{cases} \quad i = 1, 2, \dots, n. \tag{22}$$

where r_i can be given by Equation (6), and θ_i is given by

$$\theta_i = \omega_s t \tag{23}$$
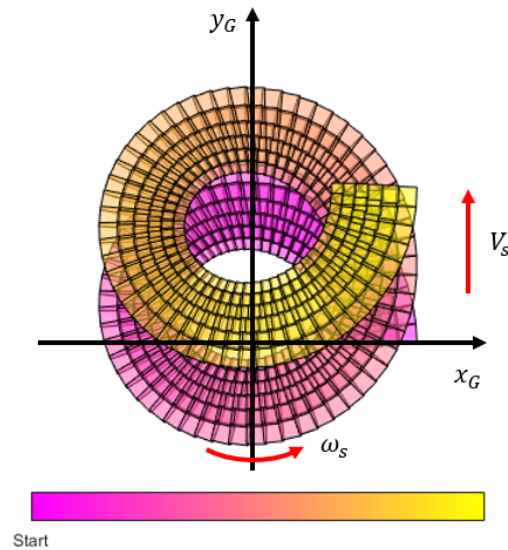
Figure 12. The schematic diagram of the OCPSI ground coverage.

According to Equation (22), it can be seen that the cone and pendulum scanning imaging is performed by three-dimensional motion coupling. In the formula, V_s represents orbital motion, θ_i represents cone scanning motion, and r_i represents pendulum scanning motion. Since the instantaneous linear velocity generated by the cone scanning on the ground at the initial moment is much greater than the velocity of the sub-satellite point caused by the orbital motion, the pendulum scanning period is changed to

$$T_{pend} = \frac{(1 - \eta_{p-cycle})d_{in}}{\omega_s r_1} \tag{24}$$

The pendulum scanning angular velocity is

$$\omega_c = \frac{2(N-1) \times \Delta\theta_{frame}}{T_{pend}} = \frac{2(N-1) \times \Delta\theta_{frame}\omega_s r_1}{\left(1 - \eta_{p-cycle}\right)d_{in}} \tag{25}$$

3.2. Dual-Camera Variable Speed OCPSI Mode

In order to reasonably plan the coverage area, reduce the overlap rate, improve the image utilization rate, reduce the pressure on the onboard data storage subsystem and data transmission subsystem, and, at the same time, reduce the requirements for the attitude control capability of the micro-nanosatellite, the dual-camera variable speed OCPSI mode is proposed.

This working mode has the advantages of the single-camera constant speed OCPSI mode, and improves some of its shortcomings. To put it simply, this working mode uses two single-chip CMOS optical cameras to distribute both sides of the satellite with the satellite nadir axis as the center. When the satellite performs cone scanning motion, the two optical cameras simultaneously perform forward or backward pendulum scanning imaging.

The sub-satellite velocity of the satellite has been calculated in Section 3.1. Then, we deduce the satellite cone scanning velocity through the dual cameras. At the initial moment, the ground coverage on the left side of the sub-satellite point is Camera 1, and the ground coverage on the right side of the sub-satellite point is Camera 2. The ground coverages of Camera 1 and Camera 2 are shown in Figure 13. The blank part of Camera 1 in the dual-camera variable speed OCPSI mode is filled by Camera 2, as shown in Figure 14.

The advantage of dual-camera variable speed OCPSI mode is that, firstly, it can offset the moment of inertia generated by the camera's swing, helping the micro-nanosatellite to adjust the attitude control. Secondly, the coverage areas of Camera 1 and Camera 2 are filled with each other, which can reduce the cone scanning velocity and the pendulum scanning velocity, thereby increasing the exposure time. At this time, the cone scanning motion period is

$$T_s = \frac{(1-\eta) \times 2(r_N - r_1)}{V_s} \tag{26}$$
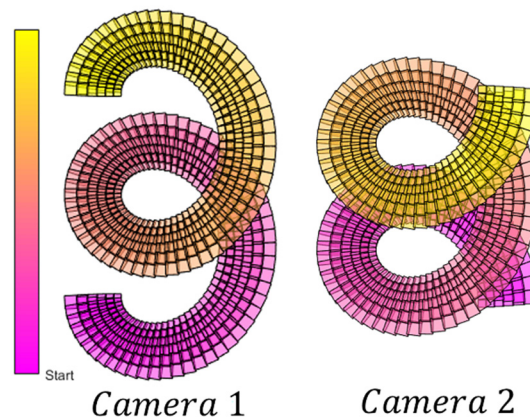
Figure 13. Dual-camera OCPSI mode overlay schematic: separate.
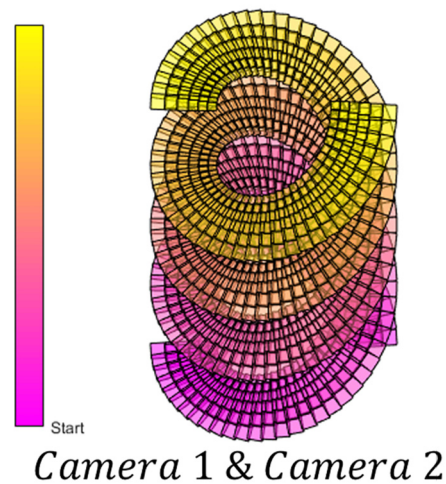
Figure 14. Dual-camera OCPSI mode overlay schematic: merging.

The cone scanning angular velocity is reduced to

$$\omega_s = \frac{2\pi}{T_s} = \frac{\pi V_s}{(1-\eta) \times (r_N - r_1)} \tag{27}$$

In order to improve the efficiency of the working mode and save the system performance, the mode is optimized by turning off some cameras and variable velocity design for some specific time periods.

First, we focus on a period of time after the start of the initial moment, and the ground cover image is shown in Figure 15. As shown, the ground cover on the swing outward is completely overlapped. Therefore, we designed the dual-camera variable speed OCPSI mode when the camera is turned off when it swings inward, and the camera is turned on for imaging when it swings outward. This can reduce the overlapping area and improve the effective utilization of the image.
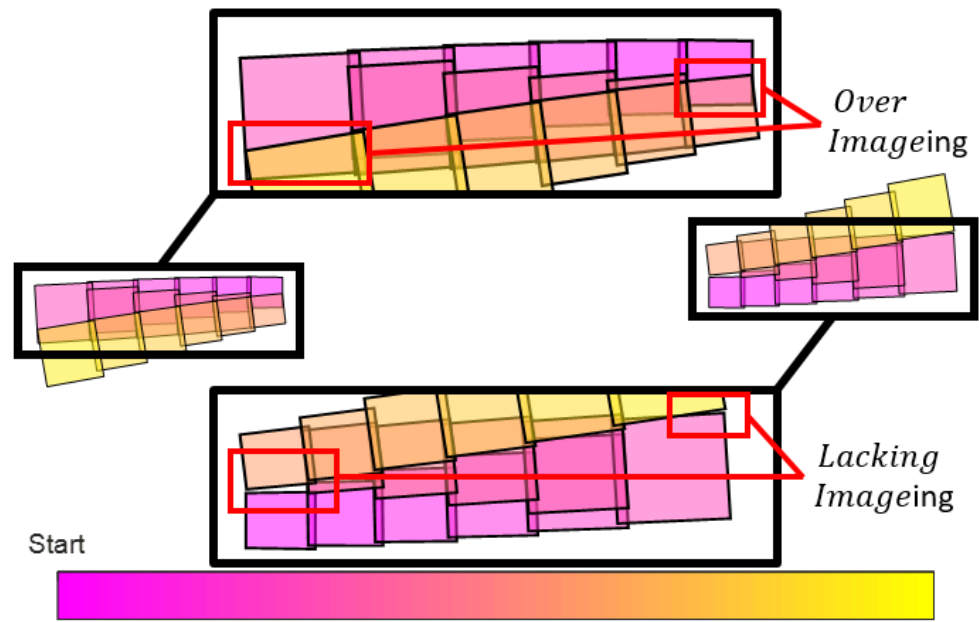
Figure 15. Image overlay diagram of the vertical rail direction.

In Figure 15, zooming in on the coverage area, the ground cover on the right has leaks, while the ground cover on the left has overlap. After the analysis, due to the indeterminate direction of the instantaneous linear velocity generated during the cone scanning, the ground on the left side is covered. That is to say, when the instantaneous linear velocity of the cone scanning is in the same direction as the velocity of the sub-satellite point, it will lead to the leakage of the ground cover during the two cycles of the pendulum scanning imaging, while the ground cover on the right side is the opposite. We have designed the variable speed mode. When the instantaneous linear velocity of the cone scanning is consistent with the direction of the sub-satellite point velocity, we reduce the pendulum scanning speed. When the instantaneous linear velocity of the cone scanning is opposite to the velocity at the sub-satellite point, we increase the sweep velocity.

Figure 16 is the ground coverage image at time t_n. At this time, we decompose the satellite sub-satellite point velocity V_s into the cone scanning tangent direction velocity V_{s1} and the cone scanning radius direction V_{s2}. As shown in the geometrical relationship in Figure 16, the pendulum scanning period becomes

$$T_{pend} = \frac{(1 - \eta_{p-cycle})d}{V_s \cos(\delta_n) + \omega_s r_1} \tag{28}$$

where d is the image block width in the tangent direction of the cone scanning circle of each frame of image, and δ_n is

$$\omega_s t_n = \delta_n - 2\pi n, \quad n = floor\left(\frac{\omega_s t_n}{2\pi}\right) \tag{29}$$

Then, the pendulum scanning angular velocity becomes

$$\omega_c = \frac{(N-1) \times \Delta\theta_{frame}}{T_{pend}} = \frac{(N-1) \times \Delta\theta_{frame}(V_s \cos(\delta_n) + \omega_s r_1)}{\left(1 - \eta_{p-cycle}\right)d} \tag{30}$$
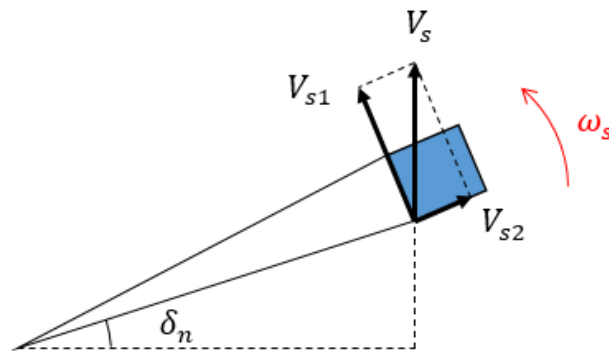
Figure 16. The ground coverage image at time t_n.

.

It can be seen from Figures 13 and 14 that the Semi-ring I of a certain cone scanning hoop, and the Semi-ring II of the next cone scanning hoop will overlap more. Therefore, we designed the two cameras to be turned on only when the semi-ring along the orbit direction—that is to say, we use the Semi-ring II of Camera 1 and the Semi-ring I of Camera 2 to overlap to form the covering strip along the orbit, as shown in Figure 17.
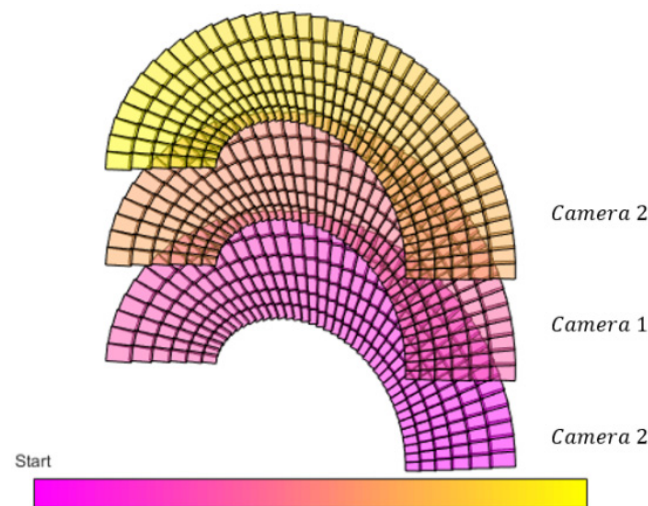

Figure 17. Dual-camera variable Speed OCPSI Mode ground overlay schematic diagram: improvement.

3.3. Derivation of Exposure Time

In order to reduce the influence of image shift, we need to plan the exposure time reasonably. Cone and pendulum scanning imaging uses motion to expand ground coverage, but this has a greater impact on image motion. The cone and pendulum scanning imaging mode adopts CMOS area array imaging. During the exposure time, the image motion amount is small enough, and the image motion influence can be ignored. The image motion amount needs to satisfy

$$t_e V_f < \mu \tag{31}$$

where t_e is the exposure time, and V_f is the image motion speed.

The orbital motion, pendulum scanning motion, cone scanning motion, and the Earth's rotation in the cone and pendulum scanning imaging mode all affect the image motion speed. If the image motion of the outermost image satisfies the requirement, then the image motion of entire images satisfies the requirement. Assuming that Figure 18 is the outermost imaging time, the outermost point of the coverage area is A, and the pixel point on the corresponding detector image surface is A'. Then, the image motion velocity can be divided into the image motion component velocity $V_{A'V_s}$ caused by orbital motion, the image motion component velocity $V_{A'\omega_s}$ caused by cone scanning motion, the image

motion component velocity $V_{A'\omega_c}$ caused by pendulum scanning motion, and the image motion component velocity $V_{A'V_e}$ of the image motion caused by the Earth's rotation.
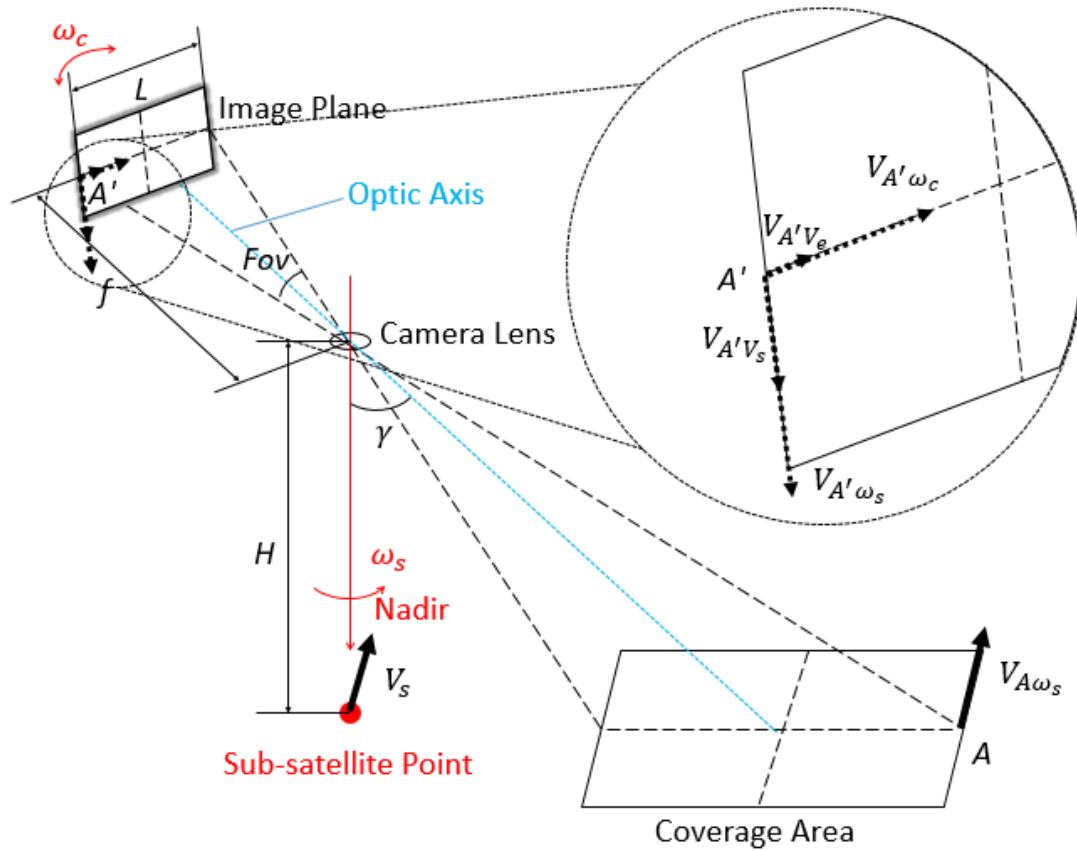

Figure 18. Image velocity analysis.

The velocity of orbital motion at the sub-satellite point is V_s. The speed and direction of the orbital motion of point A in the coverage area are the same as the satellite sub-satellite point speed V_s. The relationship between the component velocity of image motion caused by orbital motion and the velocity caused by orbital motion of point A in the coverage area is

$$\frac{V_{A'V_s}}{V_s} = \frac{f}{H / \cos\left(\gamma + \frac{FOV}{2}\right)} \tag{32}$$

Then, the component velocity of image motion caused by orbital motion is

$$V_{A'V_s} = \frac{f \cos\left(\gamma + \frac{FOV}{2}\right)}{H} \times V_s \tag{33}$$

The direction is the opposite direction along the orbit.

The angular velocity of the cone scanning motion corresponds to the linear velocity of point A in the coverage area:

$$V_{A\omega_s} = \omega_s \times r_N \tag{34}$$

Similarly, it can be deduced from the relationship between Equations (27) and (28) that the component velocity of the image motion caused by the cone scanning motion is

$$V_{A'\omega_s} = \frac{f \cos\left(\gamma + \frac{FOV}{2}\right)}{H} \times V_{A\omega s} = \omega_s f \times \frac{r_N \cos\left(\gamma + \frac{FOV}{2}\right)}{H} = \omega_s f sin\left(\gamma + \frac{FOV}{2}\right) \tag{35}$$

The direction is the circular tangent direction of the cone scanning.

Figure 19 is a cross-sectional view of the image plane A' point. The instantaneous linear velocity at the point A' of the image plane during the pendulum scanning motion is

$$V'_{\omega_c} = \omega_c \times \frac{f}{\cos(\frac{FOV}{2})} \tag{36}$$
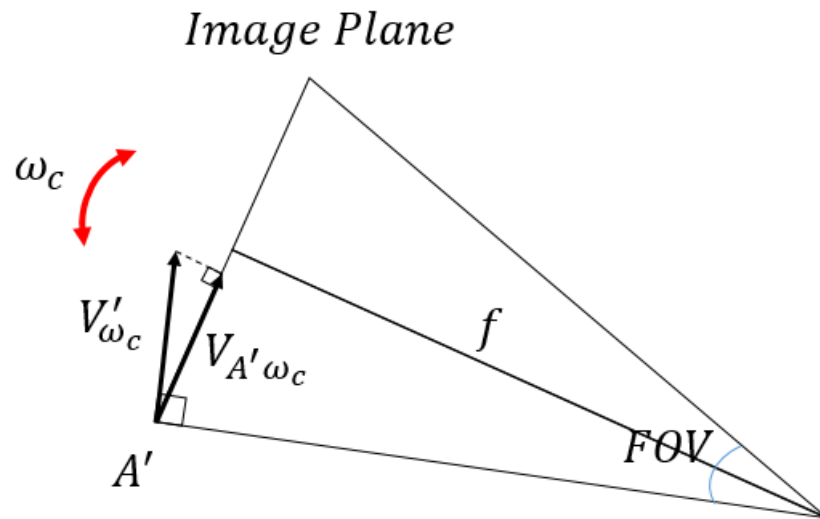
Figure 19. A cross-sectional view of the image plane A' point.

The relationship between the image motion velocity caused by the pendulum scanning motion and the instantaneous linear velocity caused by the pendulum scanning motion is shown in Figure 14, which is expressed as

$$V_{A'\omega_c} = V'_{\omega_c} \times \cos\left(\frac{FOV}{2}\right) = \omega_c f \tag{37}$$

The linear velocity of the Earth's rotation at point A in the coverage area is $V_e = 0.463 \text{ km/s}$, and the component velocity of the image movement caused by the Earth's rotation is

$$V_{A'V_e} = V_e \times \frac{f\cos^2\left(\gamma + \frac{FOV}{2}\right)}{H} \tag{38}$$

The direction is the vertical orbit direction.

According to Equations (27)–(33), the four image motion component velocities are combined into two components along the orbit and the vertical orbit. Then, the relationship of Equation (26) is satisfied, respectively, and the reasonable value of exposure time is obtained.

3.4. The Analysis of the Signal-to-Noise Ratio

In addition, the signal-to-noise ratio (SNR) is also an important parameter for evaluating image quality. The general definition of image *SNR* is the ratio of the power spectrum of the signal to the noise, which can also be expressed as the ratio of the number of signal electrons to the number of noise electrons. It can be expressed as

$$SNR = 20lg\left(\frac{S}{N}\right) \tag{39}$$

where S is the number of signal electrons, and N is the number of noise electrons.

The signal electron number is generally related to camera parameters and imaging environment and can be expressed as

$$S = \frac{\pi \cdot L \cdot \tau \cdot T_e \cdot P}{4F^2} \qquad (40)$$

where L is the entrance pupil brightness, τ is the transmittance of the optical system, T_e is the exposure time, P is the detector sensitivity, and F is the F number of the optical system.

The noise electron number of CMOS is mainly composed of shot noise, dark current noise, and transient noise, which can be expressed as

$$N = \sqrt{\sigma_{shot}^2 + T_e \cdot \sigma_{dark}^2 + \sigma_{temporal}^2} \qquad (41)$$

where σ_{shot} is shot noise, σ_{dark} is dark current noise, and $\sigma_{temporal}$ is transient noise.

Finally, the *SNR* can be expressed as

$$SNR = 20lg \left(\frac{\pi \cdot L \cdot \tau \cdot T_e \cdot P}{4F^2 \cdot \sqrt{\sigma_{shot}^2 + T_e \cdot \sigma_{dark}^2 + \sigma_{temporal}^2}} \right) \qquad (42)$$

Under the same load, only entrance pupil brightness (L) and exposure time (T_e) are variables, and *SNR* is proportional to both. The entrance pupil brightness (L) is related to the roll angle under the same sun altitude and ground reflectivity. The larger the yaw angle, the smaller the entrance pupil brightness (L).

4. Results

In this section, firstly, we present an illustrative example of this working mode through simulations. Secondly, we designed the ground verification equipment of the OCPSI mode and carried out ground verification experiments to verify the feasibility of this mode.

4.1. OCPSI Mode Simulation

Assuming that the OCPSI satellite runs on the 500-km circular sun-synchronous orbit, the satellite sub-satellite point velocity V_s is 7.057 km/s from Equation (9).

For the camera, we use a single-chip CMOS detector. The detector center is on the optical axis. It is modeled with $f = 360$ mm, $a = 2.5$ µm, $[5120 \times 5120]$, $N = 10$, $\alpha = 30°$. Here f is the focal length, a is the pixel size, $[5120 \times 5120]$ is the resolution, and N is the number of imaging frames in the pendulum scanning hoop.

According to Equations (6) and (7), we calculate $r_N = 546$ km, $r_1 = 277$ km. To guarantee the stitching is leakless in this mode, we set the overlap rate of the cone scanning hoop, the overlap rate between the pendulum scanning frames, and the overlap rate between the pendulum scanning periods to be 10%. Then, the cone scanning angular velocity is $\omega_s = 0.1831$ rad/s, the cone scanning period $T_s = 34.3175$ s, the pendulum scanning angular velocity $\omega_c = 1.8193$ rad/s, and the pendulum scanning period $T_{pend} = 0.3166$ s. The simulation results are shown in Figure 20. The black box in the figure is valid data, and it can be observed that there is no leakage in the coverage. As shown in Figure 20, the maximum width can reach 1092 km, the effective width can reach 1060 km, and the effective efficiency can reach 97%, but it can be seen that the overlap is very high. According to Equations (26)–(33), we get the exposure time $t_e = 3.79$ µs.

For remote sensing missions, the ground sampling distance (GSD) is an important mission indicator. The *GSD* is

$$GSD = \frac{al}{f} \qquad (43)$$

where l is the distance between the satellite and the ground sampling point. According to the above indicators, we get the GSD of 4.06~5.28 m. Therefore, it can be seen that the OCPSI mode can reach a coverage width of the order of 1000 km at the ground sampling distance of 5.3 m.
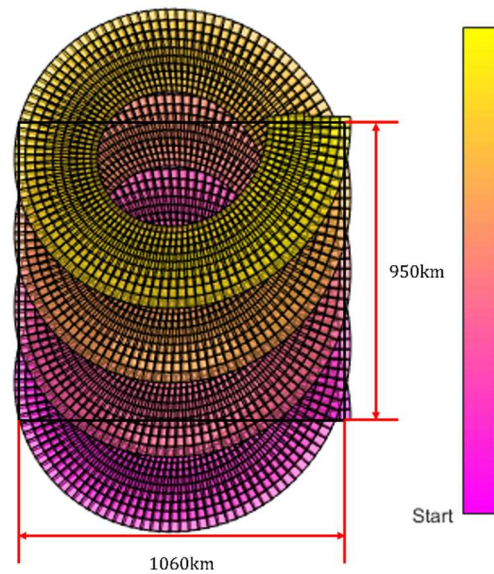
Figure 20. Single-camera constant Speed OCPSI mode ground cover simulation.

In order to obtain higher quality images and improve data utilization, a dual-camera variable speed OCPSI mode is designed according to the principle proposed in Section 3.2.

According to Equations (34) and (35), we obtain that the cone scanning angular velocity of the dual-camera variable speed OCPSI mode is 0.0915 rad/s and the cone scanning period is 68.635 s. Then, according to Equations (36)–(38), we obtain the pendulum motion angular velocity and exposure time of the dual-camera variable speed OCPSI mode, as shown in Figures 21 and 22. The pendulum motion angular velocity is reduced to 0.63–1.06 rad/s, and the exposure time is increased to 6.4–11.2 μs. This imaging mode reduces the overlap of each frame of images by changing the angular speed of the cone scanning to reduce the amount of data and improve the effective coverage of images. Therefore, the ground coverage simulation of this mode is shown in Figure 23.
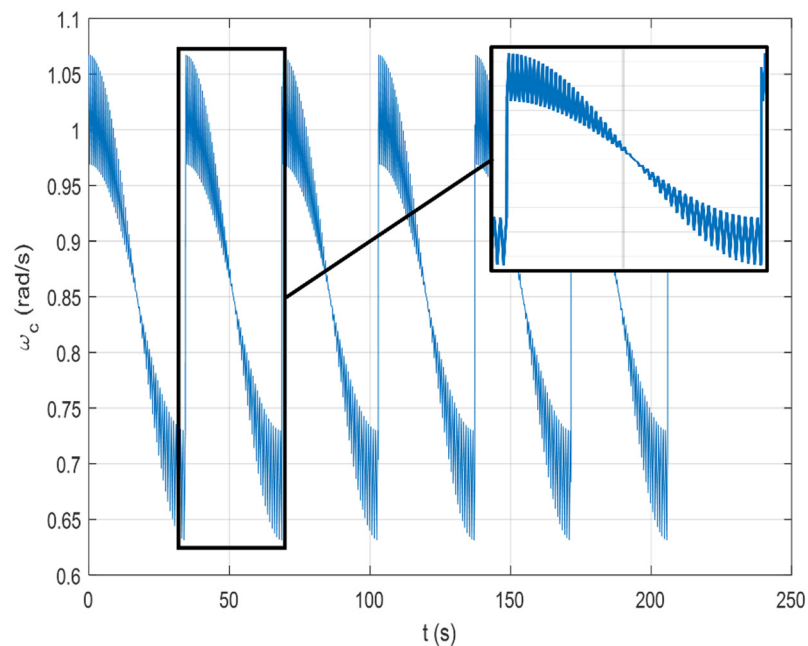
Figure 21. Dual-camera variable speed OCPSI mode: pendulum motion angular velocity.
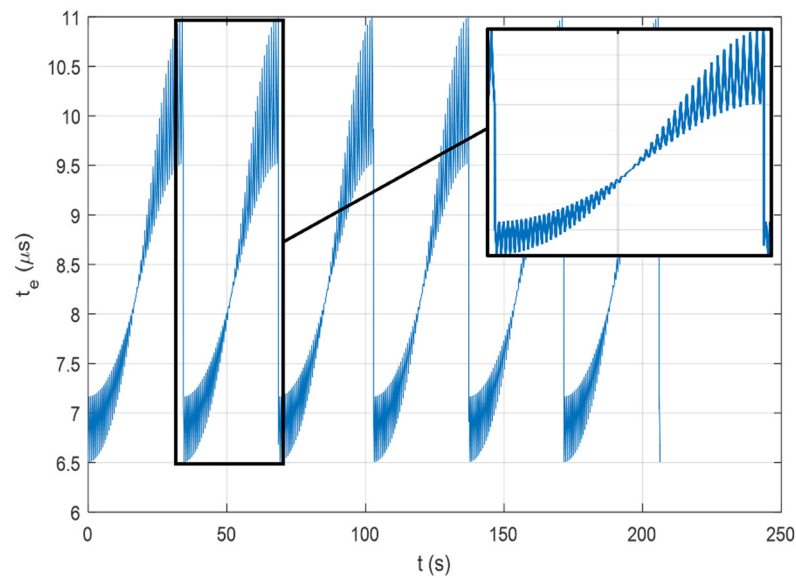
Figure 22. Dual-camera variable speed OCPSI mode: exposure time.
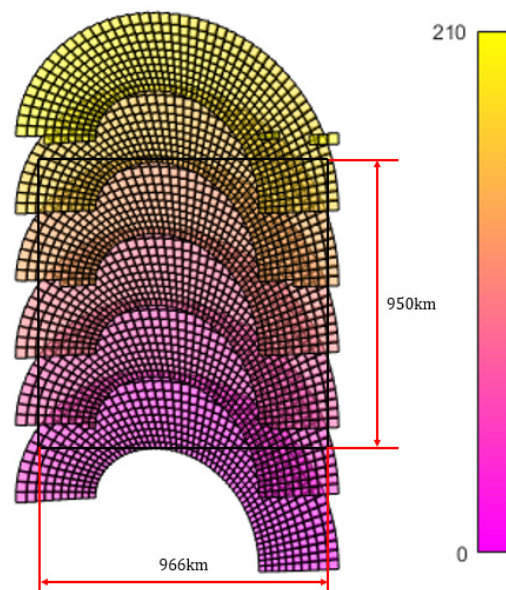
Figure 23. Dual-camera variable speed OCPSI mode ground cover simulation.

According to Figure 23, it can be seen that the ground coverage overlap is significantly reduced, but the effective width is 966 km, which is 100 km lower than that of the single-camera constant speed OCPSI mode.

Table 1 shows that dual-camera variable speed OCPSI mode effectively reduces cone scanning angular velocity and pendulum motion angular velocity. This mode improves the exposure time and image quality. However, it can be seen from Figures 20 and 23 that the ground coverage width of the dual-camera variable Speed OCPSI mode is reduced by 100 km. When the effective coverage along the track direction reaches the same range, single-camera constant speed OCPSI mode requires four cone scanning rings, while dual-camera variable speed OCPSI mode requires six cone scanning rings.

Table 1. Comparison table of related parameters of the two imaging modes.

	Cone Scanning Angular Velocity ω_s (rad/s)	Pendulum Motion Angular Velocity ω_c (rad/s)	Exposure Time t_e (μs)	Effective Width (km)
Single-camera constant speed OCPSI mode	0.1831	1.8193	3.79	1060
Dual-camera variable speed OCPSI mode	0.0915	0.6317 (min) 1.0670 (max)	6.24 (min) 11.2 (max)	966

Compared with the traditional wide-image imaging modes (multi-sensor internal field of view stitching, multi-camera outer field of view stitching, and satellite agile imaging based on satellite maneuvering ability), the OCPSI mode has obvious advantages of increasing the width while ensuring a high resolution. In recent years, other novel imaging modes, the optical conical scanning imaging mode and linear array sensors circular scanning perpendicular to the orbit imaging mode, have been proposed [28]. The optical conical scanning imaging mode adopts the method of splicing multiple sensors in the field of view to form a large detection area camera. The camera is installed obliquely, and the satellite rotates continuously to complete the coverage. Linear array sensors circular scanning perpendicular to the orbit imaging mode adopts linear array CCD (Charge Coupled Device) camera, and the satellite vertical orbit is continuously rotated to complete the coverage. Both methods can achieve 1000-km coverage on a 500-km track. However, compared with the OCPSI mode, these two methods use the method of inner field of view splicing to design the camera, and the structure of the long focal length of the large primary mirror is unavoidable in order to ensure high resolution. Therefore, their payload volume and weight are too large, which limits their application in micro-nanosatellites. Compared with the new imaging mode, the OCPSI mode has unique advantages, which can take into account the high resolution, ultra-large width, and light weight at the same time.

*4.2. Ground Verification Experiment*

In order to verify the feasibility of the OCPSI mode, we designed a ground verification device. Firstly, we choose a CMOS area array camera with a pixel size of 3.45 × 3.45 μm and the resolution of 1440 × 1080, which can support the exposure time of 1 μs~10 s and a lens with the focal length of 25 mm. Then, we use the sky rail to simulate the orbit and use three rotating mechanisms to simulate the orbital motion, the cone scanning motion, and the pendulum scanning motion. The experimental equipment is shown in Figures 24 and 25.


Figure 24. Experimental equipment: platform.

Figure 25. Experimental equipment: load system.

We use the indoor patio as the experimental site for experiments, and the height of the experimental rail is 11 m. Due to the limited indoor space, we model it as $\alpha = 10°$, $N = 3$. Since the sky rail is a soft rope with insufficient rigidity, the height of the platform will change during the operation of the platform, and the optical axis will also shift, as shown in Figure 26.
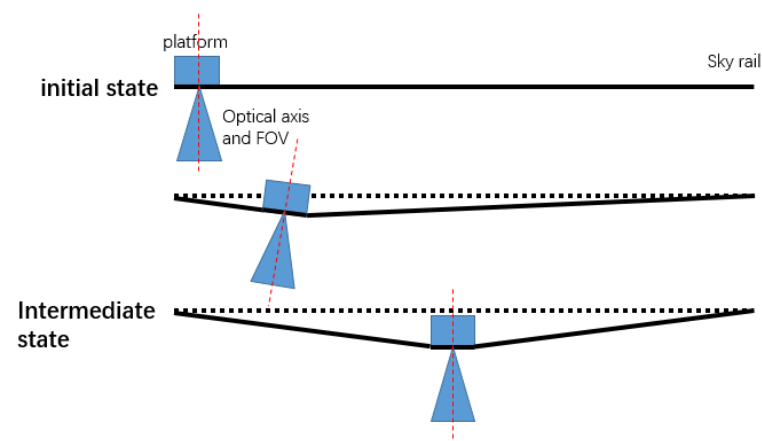

Figure 26. Operating status analysis of the experimental equipment.

We increased the overlap rate for improvement. We obtain the motion parameters of the OCPSI as the platform speed V_s is 0.04 m/s, the cone scanning speed ω_s is 4.34°/s, and the pendulum motion speed ω_c is 7.00°/s. Figure 27 is a simulation diagram of the ground experiment in the OCPSI mode, with the maximum width of 11.83 m.
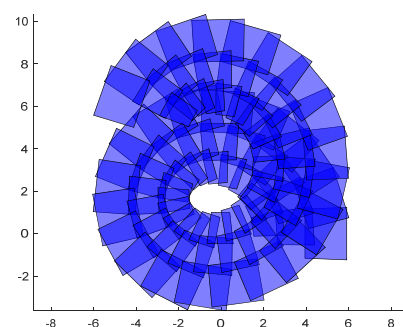
Figure 27. Simulation of ground experiment coverage in the OCPSI mode.

Image stitching is performed according to the collected images, and the experimental image is shown in Figure 28. The effective image is Figure 29, and the width reaches 10.80 m.
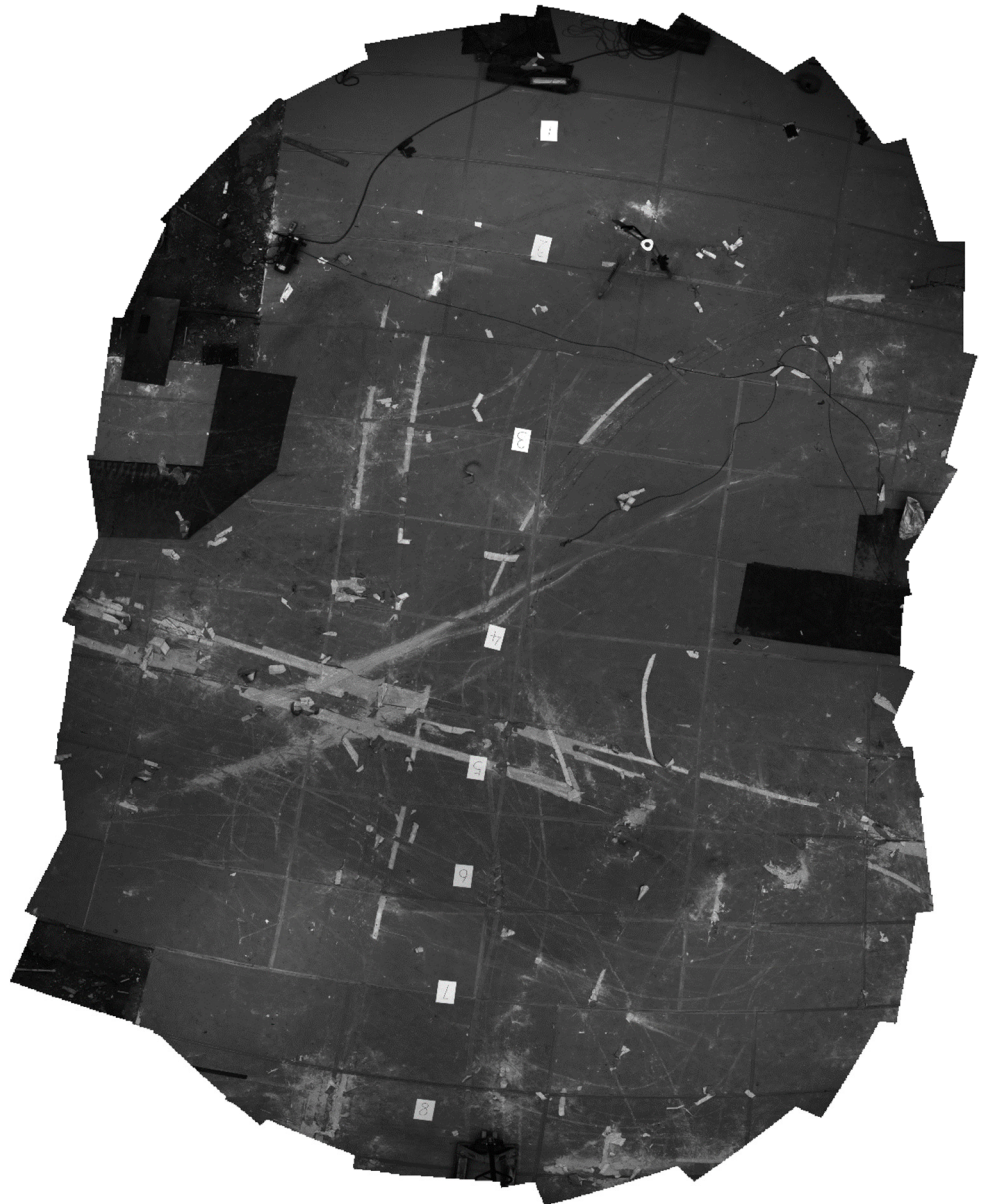
Figure 28. OCPSI mode: experimental image.

Afterwards, we conducted push-broom and whisk-broom ground experiments with the same experimental equipment and experimental conditions. Figures 30 and 31 are experimental images. The width of the push-broom is 1.64 m, and a part of the overlap is required to ensure complete coverage. To achieve the width of the OCPSI mode, at least seven tracks are required. When the whisk-broom mode adopts the same whisk-broom half-cycle frame number as the OCPSI mode and the number of frames is three frames, the whisk-broom width is 3.83 m, and at least three tracks are required to achieve the width of the OCPSI mode.
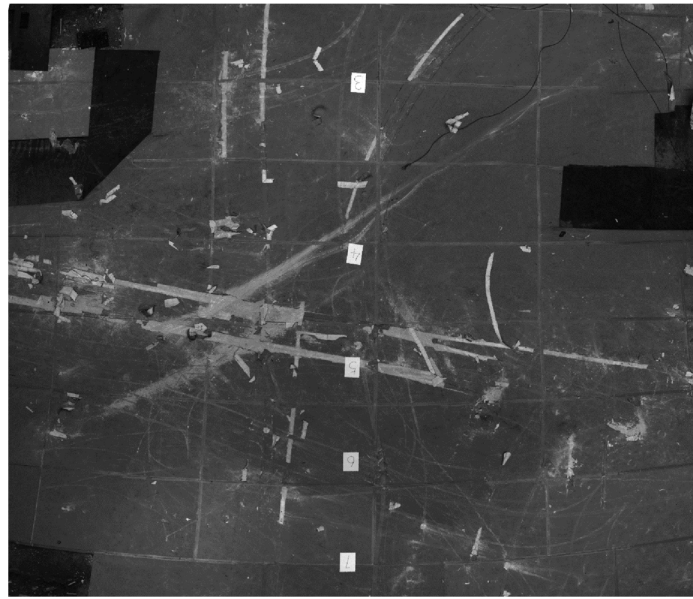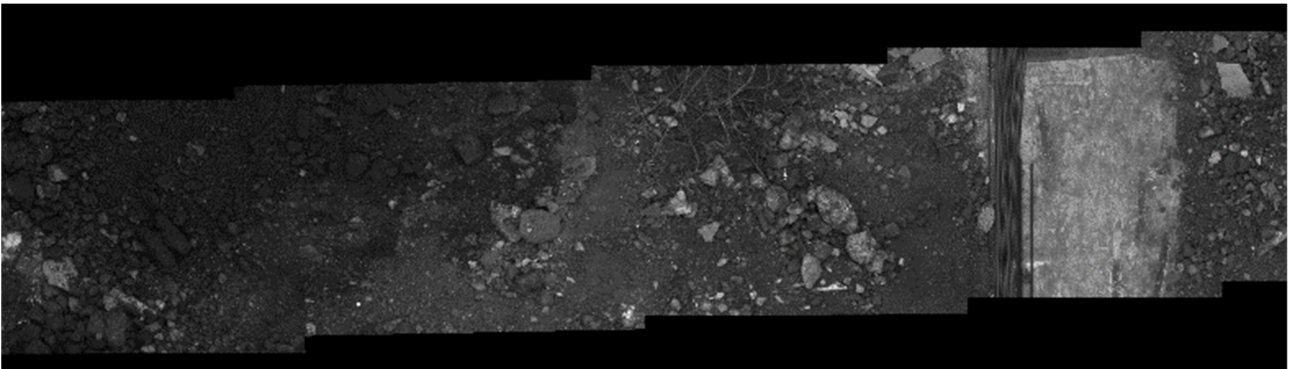
Figure 29. OCPSI mode: effective image.

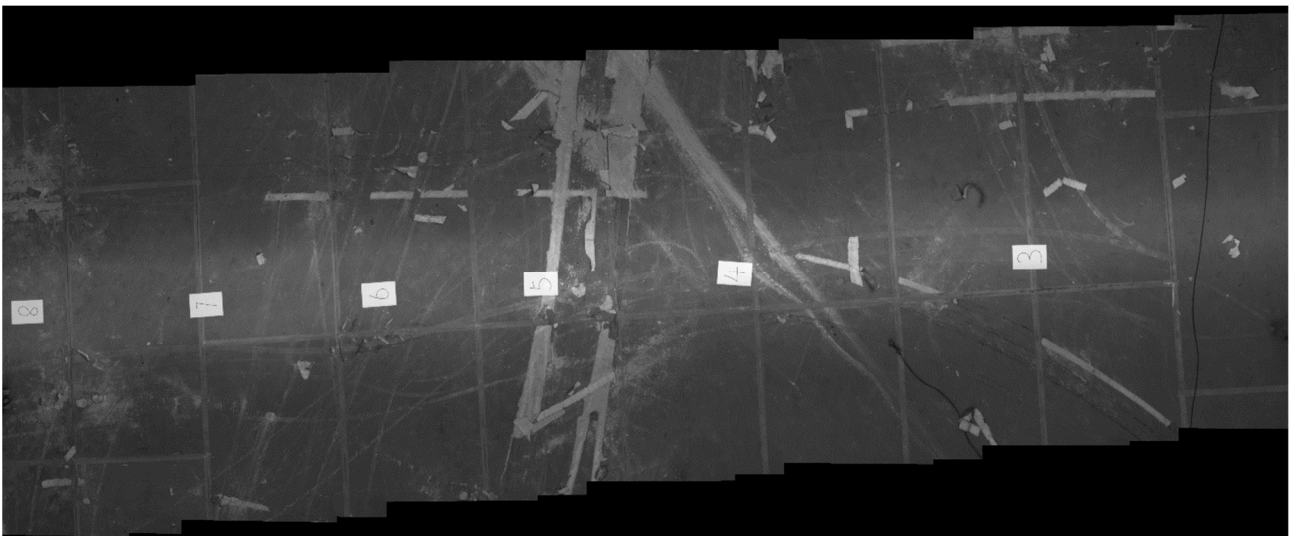**Figure 30.** Push-broom ground test cover diagram.

Figure 31. Whisk-broom ground test cover diagram.

However, compared to the push-broom mode and the whisk-broom mode, the OPCSI mode also has its limitations. The OPCSI mode has a larger roll angle (smaller entrance pupil brightness) and a smaller exposure time, so the OPCSI mode has a smaller SNR. This means that the image quality of OPCSI mode will be worse under the same conditions. In addition, due to the characteristics of in-motion imaging in OPCSI mode, the camera pendulum scanning velocity will be very fast. Compared with the push-broom mode and the whisk-broom mode, it will put forward higher requirements on the attitude control ability of the satellite platform.

In this section, we first designed and simulated a single-camera constant speed OCPSI mode. The results showed that the effective swath of this mode was large, but the overlap area was also larger, and the exposure time was low. In order to improve the cone-sweep imaging mode, we next designed and simulated the dual-camera variable speed OCPSI mode. The results showed that the overlapping area of this mode was significantly reduced, and the exposure time was increased by at least two times, but the effective width decreased. The single-camera constant speed OCPSI mode had the larger coverage area and the simpler control strategy. The dual-camera variable speed OCPSI mode had less overlapping area and better image quality. Finally, we designed the ground experiment equipment of the OCPSI mode and carried out the ground experiments of the OCPSI mode, the push-broom mode and the whisk-broom mode, and compared them. The results showed that, under the same conditions, the OCPSI mode can achieve a larger width on a single track. However, after analysis, the SNR of the OPCSI mode was smaller, and the image quality would be worse. Due to the unique motion imaging method, the camera pendulum scanning velocity would be very fast, which would put forward higher attitude control requirements for the satellite platform.

5. Conclusions

In this paper, a novel optical cone and pendulum scanning imaging mode is proposed, where in-motion imaging is adopted to break the restrictive relationship between the high resolution, wide width, and compact size of remote sensing satellites. This imaging mode uses an optical camera composed of a single CMOS sensor, allowing the camera to have an initial tilt angle to obtain ultra-wide coverage through the three-dimensional motion of the satellite and the camera. Two 3D motion imaging modes are designed, the single-camera constant speed OCPSI mode and the dual-camera variable speed OCPSI mode. Compared with each other, the control strategy of the single-camera constant speed OCPSI mode is simpler and covers a wider range, which is suitable for use in situations where too high resolution is not required. For tasks that require higher image quality, the dual-camera variable speed OCPSI mode is a better choice. Finally, numerical simulations and ground verification experiments are conducted to verify its effectiveness. The results show that, under the same conditions, the ground coverage width of the OCPSI mode is seven times wider than that of the push-broom imaging mode and three times wider than that of the whisk-broom imaging mode.

The OCPSI mode breaks the routine and applies the high-resolution camera imaging method in motion to reasonably plan the image position of each frame. Then, it adopts the frame-type splicing method, which effectively improves the single-track ground coverage width of the high-resolution optical remote sensing satellite. At the same time, due to its unique motion imaging mode, the exposure time is very short in order to ensure that the imaging quality does not suffer from severe image shift. Therefore, this imaging mode requires a large sun elevation angle, which limits its application scenarios. In addition, the too-fast the camera pendulum velocity and the attitude control ability of the micro-nanosatellite will increase the difficulty of maintaining the stability of the OCPSI satellite. As a new imaging method, the OCPSI mode still has many related topics to be studied to improve its theoretical system, such as the rational selection of camera detectors, the design optimization of camera structure and motion structure, the design of large-angle moving

image processing algorithms, the research to the promotion of the exposure time mode, and the research on the stability of the satellite platform ability.

References

1. Wang, F.; Xi, R.; Yue, C.; Li, H.; Cao, X. Conceptual rotational mode design for optical conical scanning imaging small satellites. *Sci. China-Technol. Sci.* **2020**, *63*, 1383–1395. [CrossRef]
2. Xue, Y.; Li, Y.; Guang, J.; Zhang, X.; Guo, J. Small satellite remote sensing and applications-History, current and future. *Int. J. Remote Sens.* **2008**, *29*, 4339–4372. [CrossRef]
3. Sandau, R. Status and trends of small satellite missions for Earth observation. *Acta Astronaut.* **2010**, *66*, 1–12. [CrossRef]
4. Tang, X.M.; Hu, F.; Wang, M.; Pan, J.; Jin, S.Y.; Lu, G. Inner FoV Stitching of Spaceborne TDI CCD Images Based on Sensor Geometry and Projection Plane in Object Space. *Remote Sens.* **2014**, *6*, 6386–6406. [CrossRef]
5. Wang, T.; Zhang, Y.; Zhang, Y.; Zhang, Z.; Xiao, X.; Yu, Y.; Wang, L. A Spliced Satellite Optical Camera Geometric Calibration Method Based on Inter-Chip Geometry Constraints. *Remote Sens.* **2021**, *13*, 2832. [CrossRef]
6. Qiao, G.; Wang, W.A. Geometric correction and spatial visualization of accuracy on QuickBird imagery. In Proceedings of the 14th International Conference on Geoinformatics, Wuhan, China, 15–17 November 2006.
7. Wang, M.; Cheng, Y.; Guo, B.; Jin, S. Parameters determination and sensor correction method based on virtual CMOS with distortion for the GaoFen6 WFV camera. *ISPRS J. Photogramm. Remote Sens.* **2019**, *156*, 51–62. [CrossRef]
8. Kainz, W.; Tang, X.; Xue, Y. The Austrian node of the natural resources satellite remote sensing cloud service platform: Examples of Sino-Austrian cooperation. *Geo-Spat. Inf. Sci.* **2021**, *24*, 145–151. [CrossRef]
9. Xiong, Q.; Wang, Y.; Liu, D.; Ye, S.; Du, Z.; Liu, W.; Huang, J.; Su, W.; Zhu, D.; Yao, X.; et al. A Cloud Detection Approach Based on Hybrid Multispectral Features with Dynamic Thresholds for GF-1 Remote Sensing Images. *Remote Sens.* **2020**, *12*, 450. [CrossRef]
10. Yang, F.; Fan, M.; Tao, J. An Improved Method for Retrieving Aerosol Optical Depth Using Gaofen-1 WFV Camera Data. *Remote Sens.* **2021**, *13*, 280. [CrossRef]
11. Jia, K.; Liang, S.; Gu, X.; Baret, F.; Wei, X.; Wang, X.; Yao, Y.; Yang, L.; Li, Y. Fractional vegetation cover estimation algorithm for Chinese GF-1 wide field view data. *Remote Sens. Environ.* **2016**, *177*, 184–191. [CrossRef]
12. Ghuffar, S. DEM Generation from Multi Satellite PlanetScope Imagery. *Remote Sens.* **2018**, *10*, 1462. [CrossRef]
13. Foster, C.; Hallam, H.; Mason, J. Orbit Determination and Differential-Drag Control of Planet Labs Cubesat Constellations. *arXiv* **2015**, arXiv:1509.03270.
14. Gaebler, J.A.; Axelrad, P. Identity Management of Clustered Satellites with a Generalized Labeled Multi-Bernoulli Filter. *J. Guid. Control Dyn.* **2020**, *43*, 2046–2057. [CrossRef]
15. Xu, R.; Li, Z.; Cui, P. Geometry-based distributed arc-consistency method for multiagent planning and scheduling. *Sci. China-Technol. Sci.* **2019**, *62*, 133–143. [CrossRef]
16. Aguilar, M.A.; del Mar Saldana, M.; Aguilar, F.J. Generation and Quality Assessment of Stereo-Extracted DSM from GeoEye-1 and WorldView-2 Imagery. *IEEE Trans. Geosci. Remote Sens.* **2013**, *52*, 1259–1271. [CrossRef]
17. Michel, P.; Jean-Philippe, C.; Claire, T.; Delphine, F. Potential of pleiades vhr data for mapping applications. In Proceedings of the IEEE International Geoscience and Remote Sensing Symposium (IGARSS), Melbourne, Australia, 21–26 July 2013.
18. Liu, Y.K.; Ma, L.-L.; Wang, N.; Qian, Y.-G.; Zhao, Y.-G.; Qiu, S.; Gao, C.-X.; Long, X.-X.; Li, C.-R. On-orbit radiometric calibration of the optical sensors on-board SuperView-1 satellite using three independent methods. *Opt. Express* **2020**, *28*, 11085–11105. [CrossRef]
19. Park, H.; Camps, A.; Querol, J.; Szczepankiewicz, K.; De Negueruela, C.; Oryszczak, W.; Soto, L.; Kedzierawski, R.; Roda, F.A. Generic Simulator For Conical Scanning Microwave Radiometers. In Proceedings of the 15th IEEE Specialist Meeting on Microwave Radiometry and Remote Sensing of the Environment (MicroRad), Cambridge, MA, USA, 27–30 March 2018.
20. Cherny, I.V.; Chernyavsky, G.M. Combined optical-microwave imager/sounder MTVZA-OK. In Proceedings of the IEEE International Geoscience and Remote Sensing Symposium, Univ New S Wales, Sydney, Australia, 11–16 July 2021.
21. Sethmann, R.; Burns, B.A.; Heygster, G.C. Spatial-resolution improvement of SSM/I data with image-restoration techniques. *IEEE Trans. Geosci. Remote Sens.* **1994**, *32*, 1144–1151. [CrossRef]
22. Hollinger, J.P.; Peirce, J.L.; Poe, G.A. SSM/I instrument evaluation. *IEEE Trans. Geosci. Remote Sens.* **1990**, *28*, 781–790. [CrossRef]

23. Das, N.N.; Entekhabi, D.; Dunbar, R.S.; Chaubell, M.J.; Colliander, A.; Yueh, S.; Jagdhuber, T.; Chen, F.; Crow, W.; O'Neill, P.E.; et al. The SMAP and Copernicus Sentinel 1A/B microwave active-passive high resolution surface soil moisture product. *Remote Sens. Environ.* **2019**, *233*, 111380. [CrossRef]

24. Spencer, M.; Wheeler, K.; White, C.; West, R.; Piepmeier, J.; Hudson, D.; Medeiros, J. The Soil Moisture Active Passive (SMAP) Mission L-Band Radar/Radiometer Instrument. In Proceedings of the 30th IEEE International Geoscience and Remote Sensing Symposium (IGARSS) on Remote Sensing-Global Vision for Local Action, Honolulu, HI, USA, 25–30 July 2010.

25. Kellogg, K.; Thurman, S.; Edelstein, W.; Spencer, M.; Chen, G.S.; Underwood, M.; Njoku, E.; Goodman, S.; Jai, B. NASA's Soil Moisture Active Passive (SMAP) Observatory. In Proceedings of the IEEE Aerospace Conference, Big Sky, MT, USA, 2–9 March 2013.

26. Wu, F.; Cao, X.; Butcher, E.A.; Wang, F. Dynamics and control of spacecraft with a large misaligned rotational component. *Aerosp. Sci. Technol.* **2019**, *87*, 207–217. [CrossRef]

27. Ousaloo, H.S. Attitude acquisition from an arbitrary tumbling state using two skewed reaction wheels. *Aerosp. Sci. Technol.* **2018**, *72*, 84–94. [CrossRef]

28. Xue, W.; Wang, P.; Zhong, L.-Y. Geometric correction of optical remote sensing satellite images captured by linear array sensors circular scanning perpendicular to the orbit. *Opt. Precis. Eng.* **2021**, *29*, 2924–2934. [CrossRef]